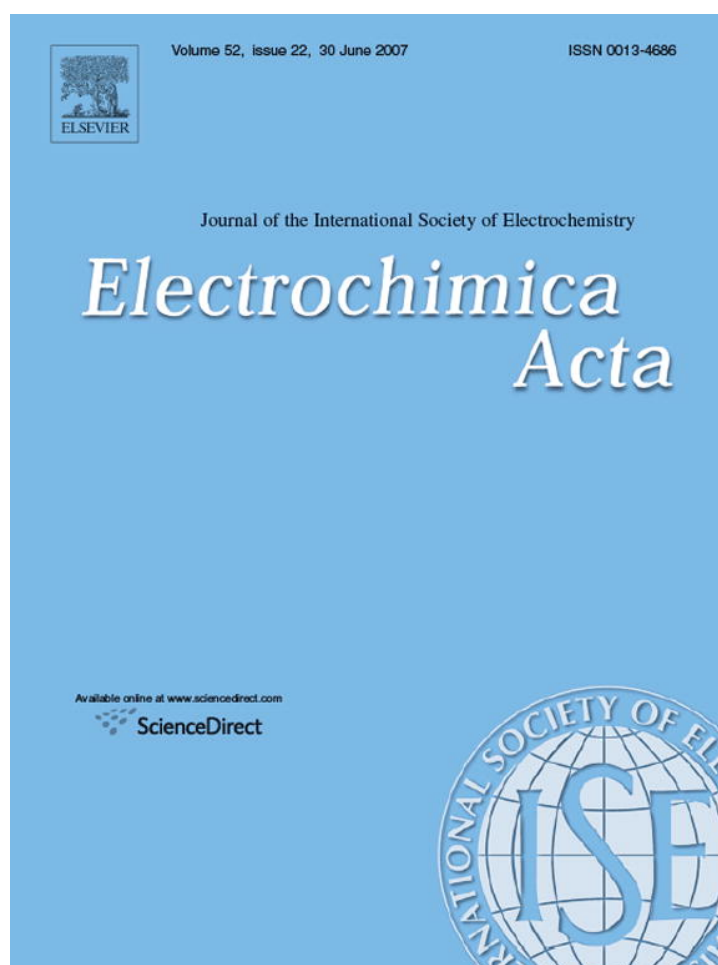


Provided for non-commercial research and educational use only.
Not for reproduction or distribution or commercial use.



This article was originally published in a journal published by Elsevier, and the attached copy is provided by Elsevier for the author's benefit and for the benefit of the author's institution, for non-commercial research and educational use including without limitation use in instruction at your institution, sending it to specific colleagues that you know, and providing a copy to your institution's administrator.

All other uses, reproduction and distribution, including without limitation commercial reprints, selling or licensing copies or access, or posting on open internet sites, your personal or institution's website or repository, are prohibited. For exceptions, permission may be sought for such use through Elsevier's permissions site at:

<http://www.elsevier.com/locate/permissionusematerial>



Optimization of polymer electrolyte fuel cell cathode catalyst layers via direct numerical simulation modeling

Guoqing Wang¹, Partha P. Mukherjee, Chao-Yang Wang*

Electrochemical Engine Center (ECEC), Department of Mechanical & Nuclear Engineering, The Pennsylvania State University, University Park, PA 16802, United States

Received 14 March 2007; received in revised form 10 April 2007; accepted 11 April 2007

Available online 25 April 2007

Abstract

The cathode catalyst layer (CL), due to sluggish oxygen reduction reaction and several transport losses therein, plays an important role in the overall performance of polymer electrolyte fuel cells (PEFCs). The relative volume fractions of the constituent phases, i.e. the electronic, electrolyte and void phases, of the cathode CL need to be selected appropriately in order to achieve an optimal balance between oxygen diffusion and proton conduction. In this work, the influence of electrolyte and void phase fractions of the cathode CL on the cell performance is investigated based on a pore-level description of species and charge transport through a random CL microstructure via the direct numerical simulation (DNS) model. Additionally, the effects of inlet relative humidity and net water transport from the anode on the cathode performance have been studied which indicate the interdependence between the CL composition and the cell operating conditions. The results indicate that the low humidity operation benefits the performance by enhancing the oxygen transport especially under high current densities. Finally, the DNS model predicts the volume fractions of 0.4 and 0.26 for the void and electrolyte phases, respectively, as the optimal composition of the catalyst layer for the best performance. © 2007 Elsevier Ltd. All rights reserved.

Keywords: PEFC; Cathode catalyst layer; Direct numerical simulation (DNS); Composition optimization

1. Introduction

The catalyst layer (CL), being the host to several competing transport mechanisms, plays a crucial role in the overall performance of a polymer electrolyte fuel cell (PEFC). In the anode CL, the hydrogen oxidation reaction (HOR) produces protons and electrons, while the oxygen reduction reaction (ORR) takes place in the cathode CL, thus producing water and waste heat. Despite significant progress, the major performance limitation in a PEFC comes from the cathode catalyst layer owing to the sluggish kinetics of the ORR as well as several mass transfer losses involving species and charge transport. Of special importance is the involvement of water transport in the cathode CL, acting as the watershed accumulating water due to ORR as well as migration from the anode side via electro-osmotic drag, and therefore holds the key to the overall performance of the PEFCs. Good

proton conductivity requires hydration of the electrolyte phase, typically Nafion[®], while excess liquid water tends to block the open pores resulting in reduced oxygen diffusion to the active reaction sites. The composition of the cathode CL, in terms of the relative volume fractions of its constituent components, plays a crucial role in maintaining a delicate balance between oxygen diffusion and proton conduction. It is, therefore, imperative to investigate the interdependence between the various transport modes and the relative composition of the constituent phases in the cathode CL for optimum performance of the PEFC.

Among the several computational modeling approaches reported in the literature, the CL is either treated as an infinitely thin interface or a macrohomogeneous porous layer. Based on the theory of volume averaging, the electrode-specific models can be further distinguished as film model, homogeneous model and agglomerate model. Springer and Gottesfeld [1], Perry et al. [2] and Eikerling and Kornyshev [3] provided several analytical and numerical solutions for the cathode catalyst layer under various conditions. Furthermore, the water transport within the cathode CL has been modeled at various levels of complexities. Notable works within the computational fuel cell dynamics

* Corresponding author. Tel.: +1 814 863 4762; fax: +1 814 863 4848.

E-mail address: cwx31@psu.edu (C.-Y. Wang).

¹ Present address: Plugpower Inc., 968 Albany-Shaker Road, Latham, NY 12110, United States.

(CFCD) framework include Wang and co-workers [4–6], Berning et al. [7] and Mazumder and Cole [8]. Wang [9] provided a comprehensive overview of the various catalyst layer models. Recently, a few CL-specific models [10–15] investigated the optimization of the cathode CLs of PEFCs in order to determine the optimal Pt loading, Nafion[®] content and CL thickness by assuming either uniformly distributed or functionally graded Nafion[®] contents and Pt loadings. However, all the above-mentioned models are based on the macroscopic description and do not address localized, pore-scale phenomena. Additionally, most of the electrode-specific models [10–15] are 1-D models. Furthermore, no model has been attempted to study CL optimization based on pore-level description of species and charge transport.

In the current work, a pore-scale model for oxygen, water vapor and proton transport through a three-dimensional, random catalyst layer microstructure is presented. This model builds upon our direct numerical simulation (DNS) model, developed in Refs. [16–18]. The primary focus of the present work is to investigate the effect of the catalyst layer composition on the cell performance based on the pore-level description of the underlying transport processes and find the optimum volume fractions of the constituent phases in order to achieve the best performance. Special emphasis is also given on elucidating the effects of inlet humidity and net water transport from the anode on the cell performance through a detailed pore-scale description of the various modes of water transport in the single phase through the cathode catalyst layer.

2. DNS model

The primary idea behind the DNS model is to solve point-wise accurate conservation equations for species and charge transport directly on the catalyst layer porous structure, which obviates the application of any effective transport properties via Bruggeman-type correlations, otherwise employed in the macro-homogeneous CL models. The DNS model, therefore, comprises of two steps: (1) the CL structure generation and (2) solution of the transport equations directly on the structure.

2.1. Catalyst layer structure generation

For the ORR to occur, the cathode catalyst layer consists of three phases: (1) the electronic phase i.e. Pt catalyst particles supported on carbon for electron conduction; (2) the electrolyte phase for proton transport; and (3) pores for oxygen and product water transport. Gottesfeld and Zawodzinski [19] provided a good overview of the catalyst layer structure and functions. In the present work, the CL is assumed to be a two-phase, porous structure consisting of a mixed electronic/electrolyte phase i.e. the solid phase and the void phase and this assumption will be justified later. Henceforth, the mixed electronic/electrolyte phase will be referred to as simply the electrolyte phase in the rest of this paper.

A purely disordered “random” CL structure, bound by the first statistical moment, i.e. porosity, is computer generated by employing a random number generator. The idea of numeri-

cal reconstruction relies on the fact that an arbitrarily complex porous structure can be defined by a discrete binary phase function, $Z(\vec{r})$, where each point, \vec{r} , within the 3-D space either belongs to the void phase or the solid phase, and is given by [20]:

$$Z(\vec{r}) = \begin{cases} 0 & \text{if } \vec{r} \text{ in the void phase} \\ 1 & \text{if } \vec{r} \text{ in the solid phase} \end{cases} \quad (1)$$

For a homogeneous porous medium, the porosity, ε , is constant and is defined as the statistical average of the phase function [20]:

$$\varepsilon = \langle Z(\vec{r}) \rangle \quad (2)$$

where angular bracket refers to statistical average. Physically, the porosity is the probability that a point is in the pore space. For a homogeneous and isotropic porous medium, “pure disorder” implies that there is no correlation between two points at a distance \vec{r} in the same phase. The numerical reconstruction, therefore, consists of generating a uniform distribution of random numbers within the interval [0,1] for each elementary unit, referred to as “voxel”, within the 3-D space and finally thresholding the distribution w.r.t. porosity so that a voxel with a random number below ε belongs to the pore space [20]. This simple reconstruction rule is employed in this study and a random CL microstructure is generated with nominal porosity of 0.36 and is shown in Fig. 1.

The pore/solid phase is further distinguished as “transport” and “dead” phase. The basic idea is that a pore phase voxel surrounded by solid phase-only voxels does not take part in species transport and hence in the electrochemical reaction and can, therefore, be treated as a “dead” pore and similarly for the electrolyte phase. However, the phase connectivity is checked by repeatedly scanning the generated structure from the membrane–CL interface to the CL–GDL interface and vice-versa for the electrolyte and void phases, respectively as elaborated in our recent work [17]. This procedure of

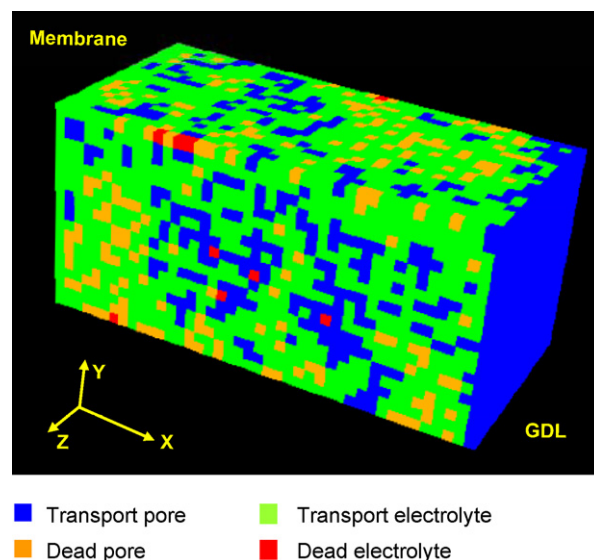


Fig. 1. 3-D random catalyst layer microstructure with nominal porosity of 0.36.

phase connectivity therefore ensures more than just 6-neighbor-connectivity for different phases. The interface between the “transport” pore and the “transport” electrolyte phases is referred to as the electrochemically active area. The impact of voxel resolution in the microstructure generation which translates directly into the number of computational cells used in the present study is elaborated in terms of the variation of resulting “transport” pore volume fraction with varying nominal porosity for different resolutions in the predecessor DNS model work in [17]. It has been observed that above a nominal porosity of 0.35, the variation of the transport pore volume fraction with increased computational unit cell resolution beyond $40 \times 20 \times 20$ cells in the thickness (x) and span-wise (y – z) directions, respectively, is negligible [17]. Since, the transport pore volume fraction and the resulting electrochemically active area are the key parameters in subsequent transport calculations, the current CL microstructure with $40 \times 20 \times 20$ unit cells can be considered adequate. Furthermore, the subsequent DNS calculations are based on one realization of the random structure generation process with the afore-mentioned unit cell resolution. In this paper, the focus is on the applicability of the DNS model in the optimization of the CL composition for improved performance. In order to obtain statistical influence of the reconstruction on transport phenomena, it is indeed imperative to consider several realizations of the generated structure. Such an investigation with an enhanced microstructure reconstruction method, with two statistical moments as inputs as described in our recent work [18], is currently underway and is envisioned to reveal some statistics of the pore-path and proton-path tortuosity of the PEFC CL structure fabricated using the catalyst coated membrane (CCM) and catalyzed diffusion medium (CDM) methods.

2.2. Transport processes and model assumptions

The key processes considered in the present study are: (1) oxygen and water vapor diffusion through the “transport” pore phase, (2) proton transport through the “transport” electrolyte phase, and (3) ORR at the electrochemically active interface.

It is important to describe the water transport mechanisms considered in the present study. Membrane hydration is ensured via the supply of externally humidified fuel and oxidant streams to the PEFC. Water is transported from the anode through the membrane by the electro-osmotic drag, expressed by:

$$N_{w,drag} = n_d N_{H^+} = n_d \times \frac{I}{F} \quad (3)$$

The electro-osmotic drag coefficient, n_d , denotes the number of water molecules carried by each proton (H^+) across the membrane as current is passed and varies in a wide range depending on different degrees of membrane hydration according to the experimental measurements by Zawodzinski et al. [21]. In the present study, a constant drag coefficient of unity is used because the water content of interest ranges from zero to 14 for a partially hydrated membrane. The water generation in the cathode CL due to ORR results in water back diffusion to the anode across the membrane owing to the concentration gradient. At higher current densities, the excessive water produced at the cathode

is removed via evaporation by the under-saturated air stream, and the removal rate can be controlled by adjusting the inlet air humidity and flow rate through the flow field.

The primary assumptions made in the current DNS model are: (1) isothermal and steady state operation; (2) negligible O_2 diffusion resistance through the polymer electrolyte film covering Pt sites due to the small thickness of the film (~ 5 nm) and existence of thermodynamic equilibrium at the reaction interface between the oxygen concentration in the gas phase and that dissolved in the electrolyte phase; (3) uniform electronic phase potential since the electrode is very thin and its electronic conductivity is very high and hence the electron transport is not considered. The ionic conductivity of the mixed phase is thus adjusted using Bruggeman correction to take into account the effect of the electronic phase volume fraction as follows [18]:

$$\kappa = \kappa_0 \left(\frac{\varepsilon_e}{\varepsilon_e + \varepsilon_s} \right)^{1.5} = \kappa_0 \left(\frac{\varepsilon_e}{1 - \varepsilon_g} \right)^{1.5} \quad (4)$$

where κ_0 is the intrinsic conductivity of the electrolyte phase, ε_e , ε_s and ε_g , are the electrolyte phase, electronic phase and gas pore volume fractions, respectively; (4) water is in the gas phase even if water vapor concentration slightly exceeds the saturation value corresponding to the cell operation temperature (i.e. slight oversaturation is allowed); and (5) water in the electrolyte phase is in equilibrium with the water vapor, thus only the water transport through the gas phase is considered and water electro-osmotic drag through the electrolyte phase in the CL is neglected.

2.3. Governing equations

The conservation equations for the transport of proton, O_2 and water, respectively, can be expressed as follows [18]:

$$\nabla \cdot (\kappa_e \nabla \phi_e) + a \int_{\Gamma} j \delta(x - x_{interface}) ds = 0 \quad (5)$$

$$\nabla \cdot (D_{O_2}^g \nabla c_{O_2}) + a \int_{\Gamma} \frac{j}{4F} \delta(x - x_{interface}) ds = 0 \quad (6)$$

$$\nabla \cdot (D_{H_2O}^g \nabla c_{H_2O}) + a \int_{\Gamma} \frac{j}{2F} \delta(x - x_{interface}) ds = 0 \quad (7)$$

where a represents the specific interfacial area and is defined as the interfacial surface area where the reaction occurs per unit volume of the catalyst layer, s is the non-dimensional interface, Γ represents the interfacial surface over which the surface integral is taken, $\delta(x - x_{interface})$ is a delta function which is zero everywhere but unity at the interface where the reaction occurs. The second term in the above equations, therefore, represents a source/sink term at the catalyzed interface where the electrochemical reaction takes place. It is important to note that the transfer current density, j , is negative for the electrolyte phase potential equation.

Based on the single-domain approach, the above governing equations are extended to be valid for the entire computational domain by introducing a discrete phase function. The phase function, f , at each elementary cell center (i, j, k), is defined as

follows [18]:

$$f(i, j, k) = \begin{cases} 0 & \text{“transport” pores} \\ 1 & \text{“transport” electrolytes} \\ 2 & \text{“dead” pores} \\ 3 & \text{“dead” electrolytes} \end{cases} \quad (8)$$

With this phase function, the proton conductivity, oxygen diffusivity and water vapor diffusivity can be recast in a discrete fashion as [18]:

$$K(i, j, k) = \frac{\kappa_e \times f(i, j, k) \times [2 - f(i, j, k)] \times [3 - f(i, j, k)]}{2} \quad (9)$$

$$D_{O_2}(i, j, k) = \frac{D_{O_2}^g \times [1 - f(i, j, k)] \times [2 - f(i, j, k)] \times [3 - f(i, j, k)]}{6} \quad (10)$$

$$D_{H_2O}(i, j, k) = \frac{D_{H_2O}^g \times [1 - f(i, j, k)] \times [2 - f(i, j, k)] \times [3 - f(i, j, k)]}{6} \quad (11)$$

The phase function is chosen such that the species diffusivity and proton conductivity identically go to zero in “dead” pore and “dead” electrolyte cells, respectively. Details about the discrete forms of the source/sink terms in the conservation equations, Eqs. (5)–(7), in terms of the phase function and electrochemical reaction at the active interface can be found in [18]. Due to the slow kinetics of the ORR, the transfer current at the electrochemically active interface is expressed by Tafel kinetics as [18]:

$$j = i_0 \frac{c_{O_2}(i+1, j, k)}{c_{O_2,ref}^g} \exp \left[\frac{\alpha_c F}{RT} \phi_e(i, j, k) \right] \quad (\text{A/cm}^2) \quad (12)$$

It should be noted that the electrochemically active interface is between the electrolyte cell (i, j, k) and the pore cell $(i+1, j, k)$ and is schematically illustrated in Fig. 2. The cathode overpotential, η , is expressed in terms of the electrolyte phase potential, $\phi_e(i, j, k)$, in the kinetic expression since both the open-circuit potential, U_0 , and the electronic phase potential, ϕ_s , are constant. However, it is worth mentioning that i_0 represents the modified exchange current density after expressing the overpotential, η ,

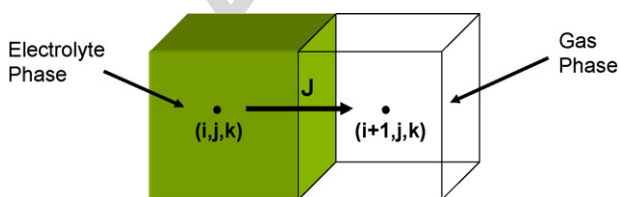


Fig. 2. Schematic of the transfer current between two adjacent cells with a catalyzed interface.

in terms of phase potential and open circuit potential as given by:

$$\eta = \phi_s - \phi_e - U_0 \quad (13)$$

2.4. Boundary conditions

At the membrane–CL interface (i.e. the left boundary) and at the CL–GDL interface (i.e. at the right boundary), one layer of electrolyte-only and pore-only cells are added to the computational domain, respectively, for ease of implementation of the boundary conditions. In the y and z directions, symmetry boundary conditions are applied. In summary, the boundary conditions are as follows [18]:

$$y = 0, \quad y = y_L, \quad z = 0, \quad z = z_L, \\ \frac{\partial c_{O_2}}{\partial n} = 0, \quad \frac{\partial c_{H_2O}}{\partial n} = 0, \quad \frac{\partial \phi_e}{\partial n} = 0 \quad (14)$$

$x = 0$ (i.e. membrane–CL interface),

$$\frac{\partial c_{O_2}}{\partial n} = 0, \quad \frac{\partial c_{H_2O}}{\partial n} = -\frac{N_{w,net}}{D_{H_2O}}, \quad -\kappa \frac{\partial \phi_e}{\partial n} = I \quad (15)$$

$x = x_L$ (i.e. CL–GDL interface),

$$c_{O_2} = c_{O_2,0}, \quad c_{H_2O} = c_{H_2O,0}, \quad \frac{\partial \phi_e}{\partial n} = 0 \quad (16)$$

The oxygen concentration at the CL–GDL interface is evaluated using the oxygen concentration in the gas channel and duly adjusting it with respect to the diffusion resistance through the GDL. The oxygen concentration in the gas channel is assumed constant, thus representative of a physically large stoichiometric flow rate. The oxygen concentration at the CL–GDL interface is given by [18]:

$$c_{O_2,0} = c_{O_2,inlet} - \frac{I \times \Delta X_{GDL}}{4F \times D_{O_2,GDL}^{g,eff}} \quad (17)$$

The oxygen concentration profile through the GDL is assumed linear and $D_{O_2,GDL}^{g,eff}$ is the effective diffusion coefficient of oxygen adjusted with respect to the GDL porosity, ε_{GDL} and tortuosity, τ_{GDL} and is given by:

$$D_{O_2,GDL}^{g,eff} = D_{O_2}^g \times \frac{\varepsilon_{GDL}}{\tau_{GDL}} \quad (18)$$

The GDL tortuosity is selected such that the diffusion resistance in the GDL is adequate to produce the resulting oxygen concentration at the CL–GDL interface and corresponding limiting current density typically observed.

At the membrane–CL interface, a net water transport coefficient, α , is employed, which takes into account the net water flux across the membrane due to the electro-osmotic drag and back diffusion effects, and can be expressed as:

$$N_{w,net} = \alpha \times \frac{1}{F} = N_{w,drag} - N_{w,dif} \quad (19)$$

where $N_{w,dif}$ is the water flux through the membrane due to back diffusion from the cathode side to the anode side. In the present study, α is assumed to be constant although it depends on a number of parameters including the cell temperature, humidity conditions at anode and cathode inlets, to name a few. Thus the boundary condition at the membrane–CL interface is given by:

$$\frac{\partial c_{H_2O}}{\partial x} \Big|_{x=0} = \frac{-N_{w,net}}{D_{H_2O}^g} \quad (20)$$

At the CL–GDL interface, water vapor concentration is calculated from the concentration of water vapor at the channel inlet with correction for diffusion resistance in the GDL and is given by [18]:

$$c_{H_2O}|_{x=x_L} = c_{H_2O,inlet} + N_{w}|_{x=x_L} \cdot \frac{\Delta X_{GDL}}{D_{H_2O,GDL}^{g,eff}} \quad (21)$$

Similar to the boundary condition treatment for oxygen transport, linear water vapor profile in the GDL and constant water vapor concentration in the gas channel are assumed. The effective diffusion coefficient of water vapor in the gas phase through the GDL is evaluated similarly as the oxygen diffusion coefficient given by Eq. (18). The water flux through the GDL is the sum of the net flux across the membrane and the water production rate in the catalyst layer and can be expressed as:

$$N_{w}|_{x=x_L} = N_{w,net} + N_{w,prod} = (\alpha + 0.5) \times \frac{1}{F} \quad (22)$$

From the inlet relative humidity, RH, water vapor concentration of the humidified air at the channel inlet is calculated by:

$$c_{H_2O,inlet} = RH \times c_{H_2O}^{sat} \quad (23)$$

where $c_{H_2O}^{sat}$ is the saturation concentration of water at the cell operating temperature.

2.5. Input parameters

The species diffusivity, D_i^g , is calculated from the specified inlet pressure, p , and temperature, T , as [22]:

$$D_i^g = D_{i,0}^g \left(\frac{p_0}{p} \right) \left(\frac{T}{T_0} \right)^{3/2} \quad (24)$$

In the present study, the reference pressure, p_0 , is taken as 1 atm and the reference temperature, T_0 as 273 K.

Based on the experimental correlation by Springer et al. [23], the proton conductivity in the electrolyte phase is given by:

$$\kappa_{e,0}(\lambda) = 100 \exp \left[1268 \left(\frac{1}{303} - \frac{1}{T} \right) \right] (0.005139\lambda - 0.00326) \quad (25)$$

where the water content in the membrane phase, λ , depends on the water activity, a , in the gas phase according to the following experimental data fit:

$$\lambda = \begin{cases} 0.043 + 17.81a - 39.85a^2 + 36.0a^3 & \text{for } 0 < a \leq 1 \\ 14 + 1.4(a - 1) & \text{for } 0 < a \leq 3 \end{cases} \quad (26)$$

Table 1
Model input parameters

Parameter	Value
Reference intrinsic oxygen diffusivity, $D_{O_2}^g$, (m ² /s)	1.8×10^{-5}
Reference intrinsic water vapor diffusivity, $D_{H_2O}^g$, (m ² /s)	1.1×10^{-5}
Pressure at the channel inlet, p (kPa)	150
Operating temperature, T (°C)	80
Thickness of the GDL, ΔX_{GDL} (μm)	300
Porosity of the GDL, ε_{GDL}	0.4
Tortuosity of the GDL, τ_{GDL}	4
Nominal porosity of the catalyst layer, ε_g	0.36
Electrolyte volume fraction in the catalyst layer, ε_e	0.3

The water activity, a , is defined as:

$$a = \frac{c_{H_2O}}{c_{H_2O}^{sat}} \quad (27)$$

The saturation pressure of water vapor is only a function of temperature, which has been formulated by Springer et al. [23] as:

$$\log_{10} p^{sat} = -2.1794 + 0.02953(T - 273.15) - 9.1837 \times 10^{-5}(T - 273.115)^2 + 1.4454 \times 10^{-7}(T - 273.15)^3 \quad (28)$$

where pressure is in bar. Substituting Eq. (26) into Eq. (25), the dependence of proton conductivity on water activity can be calculated. Thus the proton conductivity of the electrolyte phase varies with the water concentration in the catalyst layer.

Other relevant model input parameters used in the current study are summarized in Table 1.

2.6. Numerical methodology

The conservation equations, Eqs. (5)–(7), are discretized using a finite volume approach [24] and solved using the commercial CFD software Fluent[®] [25]. The user defined function (UDF) capability in Fluent[®] [25] is deployed to customize the source terms and to solve the set of governing equations within the generic framework of scalar transport equations. In the present study, for the (10 μm × 5 μm × 5 μm) random CL structure, the number of cells within the computational domain in the x , y and z directions were taken as 40 × 20 × 20, respectively, as mentioned earlier and were found to be sufficient for a realistic description of the microstructure [17]. Convergence was considered achieved when the relative error between two consecutive iterations reached 10^{-6} for each scalar field. A typical simulation for a particular current density, on a DELL PC with Pentium 4 processor, 1 GB RAM, 2.79 GHz processor speed, takes approximately 20 min to converge.

3. Results and discussion

3.1. Predicted polarization curve

The simulated polarization curve with air as the oxidant at 100% inlet relative humidity with inlet pressure of 150 kPa and

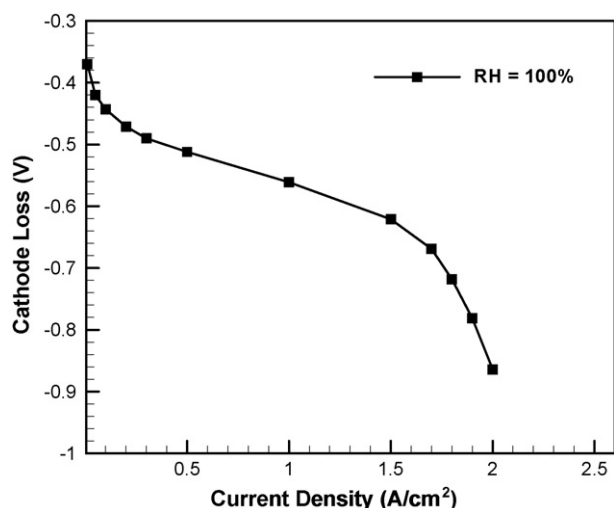


Fig. 3. Polarization curve predicted by the DNS calculation.

cell temperature of 80 °C is shown in Fig. 3. In the present study, the “polarization curve” refers to the cathode overpotential versus current density curve, thereby differing from the standard cell voltage versus current density description otherwise used popularly in the fuel cell literature. As a general trend, the predicted cathode polarization curve depicts a fast drop in the small current density region controlled by the ORR kinetics followed by a linear voltage drop in the mixed control regime and finally at higher current densities ($>1.5 \text{ A/cm}^2$), the mass transport limitation appears with a fast voltage drop resulting from oxygen depletion. Overall, Fig. 3 demonstrates that the current pore-scale DNS model is able to capture the general trend of the fuel cell performance curve on a random CL microstructure. In the present study, one realization of the generated.

3.2. Effect of inlet air humidity on performance

Fig. 4 exhibits the predicted polarization curves with air as the oxidant for inlet relative humidity of 5%, 50% and 100%.

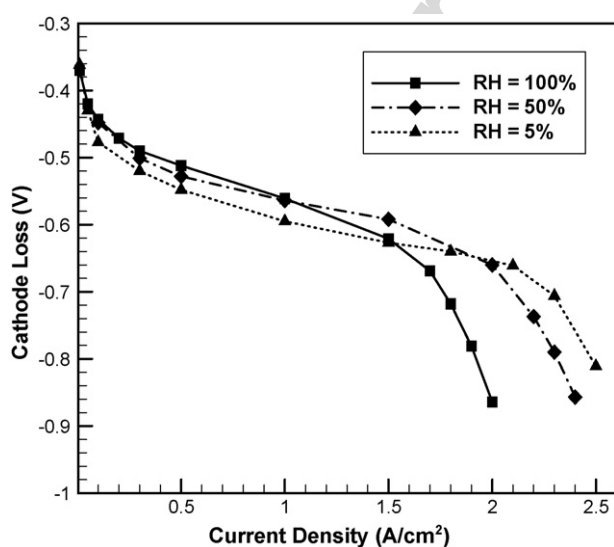


Fig. 4. Polarization curves for various inlet humidity.

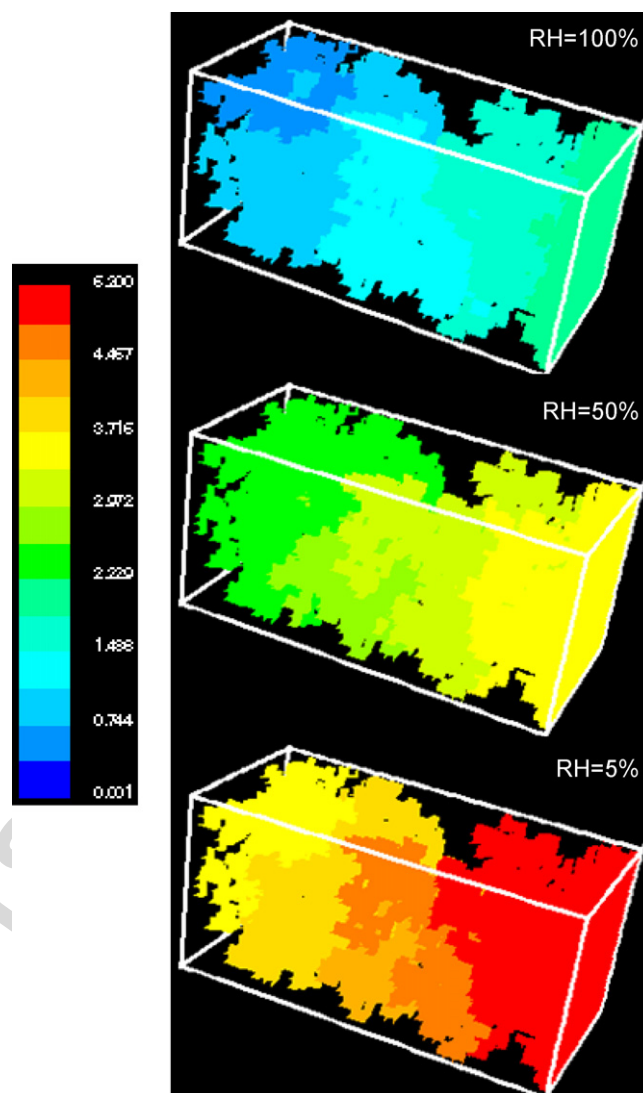


Fig. 5. 3-D oxygen concentration contours at 1.5 A/cm^2 for inlet air humidity of 100%, 50% and 5%.

As can be observed, within the kinetic control regime the cathode performance is very similar for different inlet humidity. The only factor influencing the kinetic loss is the oxygen concentration inside the catalyst layer. It can be estimated using Eq. (17) that the oxygen concentrations at the CL–GDL interface are 7.5 mol/m^3 , 9.2 mol/m^3 and 10.7 mol/m^3 for 100%, 50%, and 5% inlet air humidity, respectively. These differences in oxygen concentration bring about only minor variations in the kinetic loss. With Tafel slope of 70 mV/dec, for 100% inlet relative humidity, the kinetic loss is only 10 mV higher than that for 5% inlet RH.

It can also be observed that lower inlet humidity tends to extend the ohmic control regime, thereby postponing the onset of mass transport limitation. This is the salient advantage of low-humidity operation, which is further illustrated by the oxygen concentration field at 1.5 A/cm^2 in Fig. 5. At 100% RH, the oxygen concentration near the membrane–CL interface is as low as 0.2 mol/m^3 and the region is about to be depleted of oxygen. Correspondingly, the polarization

curve exhibits a sharp drop at a current density greater than 1.5 A/cm^2 .

However, the striking disadvantage of low-humidity operation is the larger voltage loss in the ohmic control regime. This is due to the lower proton conductivity associated with the partially hydrated electrolyte phase, leading to increased protonic resistance. At 100% RH, the electrolyte phase remains fully humidified with saturated water vapor concentration of 15.9 mol/m^3 at 80°C throughout the CL. In comparison, the water vapor concentration fields at 50% and 5% RH are shown in Fig. 6 at 0.5 A/cm^2 . It can be observed that at 50% RH the water vapor concentration is still maintained at around 10 mol/m^3 while it becomes extremely low for 5% RH, thus causing a significant increase in ohmic loss. This can be further illustrated with the variations in reaction current and overpotential distributions with inlet RH as shown in Fig. 7. It can be found that the reaction zone shifts closer to the membrane–CL interface with lower RH. Apparently, this is due to poorer proton conductivity or higher ohmic resistance in the electrolyte phase and results in a much lower surface overpotential at the back end i.e. closer to the CL–GDL interface of the CL, making the overpotential distribution more non-uniform. In order to compensate for the lower reaction current produced near the back end of the catalyst layer, the front end, i.e. closer to the membrane–CL interface, must provide higher reaction current as the average current density is fixed. This leads to a higher surface overpotential needed at the front end of the layer, representing a higher total voltage loss of the cathode under low-humidity operation.

Overall, 50% appears to be the optimal relative humidity for the catalyst layer configuration modeled here. It has a large

ohmic control range at the minimum expense of kinetic loss. It should be noted that since the present model only considers water transport in the gas phase, the salient advantage of low-humidity operation to alleviate cathode flooding cannot be demonstrated.

3.3. Effect of net water transport coefficient (α)

In the present DNS model, the net water flux through the polymer membrane to the cathode catalyst layer is estimated using the net water transport coefficient, α , as expressed by Eq. (19). The value of this coefficient reflects the contribution of water transferred from the anode to the cathode. It depends on the humidity condition on the anode side. Low value of α indicates strong back diffusion from the cathode, which means a relatively dry condition in the anode. When α is close to its maximum value, 1.0, it implies that the water flux due to electro-osmotic drag is dominant and the back diffusion is negligible. Therefore, by studying the effect of the net water transport coefficient, we can understand the influence of anode gas humidification on the cathode catalyst layer performance.

Two scenarios with net water transport coefficient of 0.2 and 0, are investigated at two different cathode inlet humidity conditions, e.g. 50% and 5% RH. Fig. 8 shows the polarization curves of the cathode pertaining to the afore-mentioned operating conditions. It can be found that for 50% RH, the value of α has negligible influence on the cathode voltage loss. The greatest difference of about 15 mV occurs at 1.5 A/cm^2 . At operating current densities greater than 1.5 A/cm^2 , the cathode performance hardly changes, which indicates that the cathode side is already sufficiently humidified due to the large water production rate even if there is no water transport from the anode. However, with the cathode inlet humidity of 5%, the value of α becomes significantly important especially at large current densities. The possible explanation is that the cathode is largely dry and hence any water supply from the anode is beneficial in increasing the proton conductivity of the electrolyte phase. To unveil the differ-

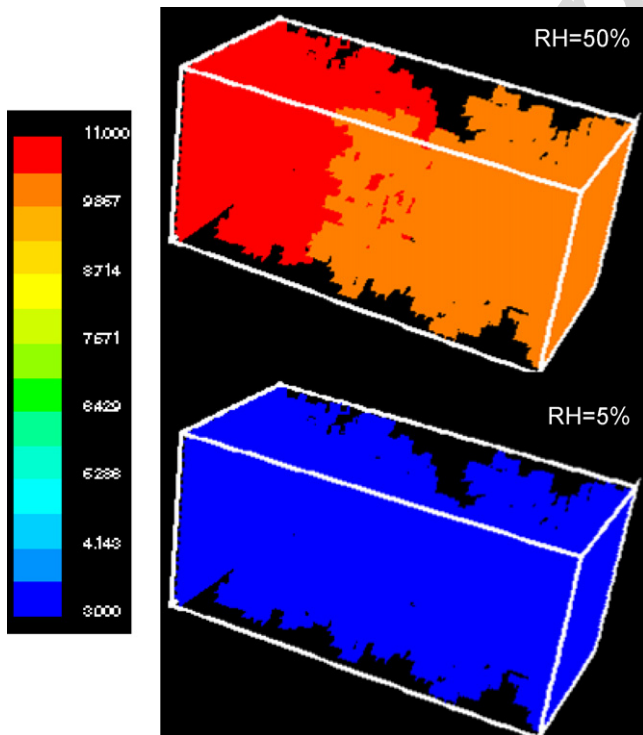


Fig. 6. 3-D water vapor concentration contours at 0.5 A/cm^2 for inlet air humidity of 50% and 5%.

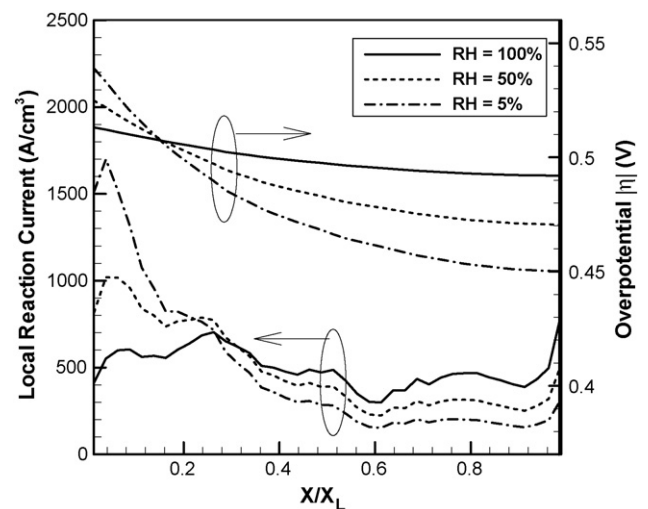


Fig. 7. Overpotential and reaction current distributions for different inlet air humidity.

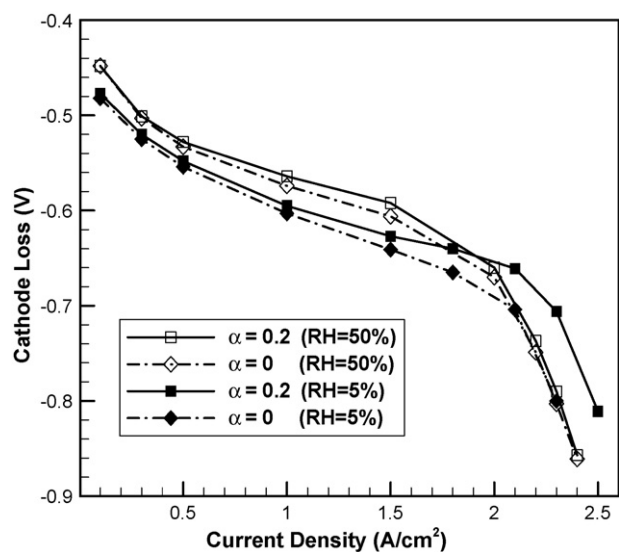


Fig. 8. Polarization curves with different net water transport coefficients at inlet humidity of 50% and 5%.

ent behaviors caused by the gas humidification, the water activity and proton conductivity distributions at 2.3 A/cm² are shown in Fig. 9.

Fig. 9 shows that both at 50% and 5% RH, the increase in the water activity with the value of α from 0 to 0.2 is the same because they are at the same operating current density which leads to the same net water flux from the anode and water production rate in the cathode. But at the cathode inlet humidity of 50%, the water activity already reaches unity (i.e. saturation) everywhere with α equal to zero. This explains why further increase of the water activity with a higher value of α (i.e. $\alpha = 0.2$) does not increase the proton conductivity further since the electrolyte phase is already fully humidified. On the other hand, at 5% RH, not only the proton conductivity is much lower, but also the difference in the conductivity under different net water fluxes is much larger. The effect of net water transport coefficient is

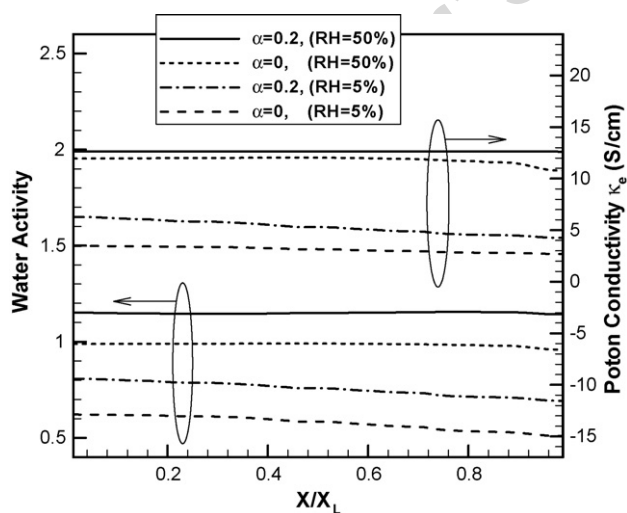


Fig. 9. Cross-section averaged water activity and proton conductivity distributions across the catalyst layer thickness at 2.3 A/cm² for different net water transport coefficients.

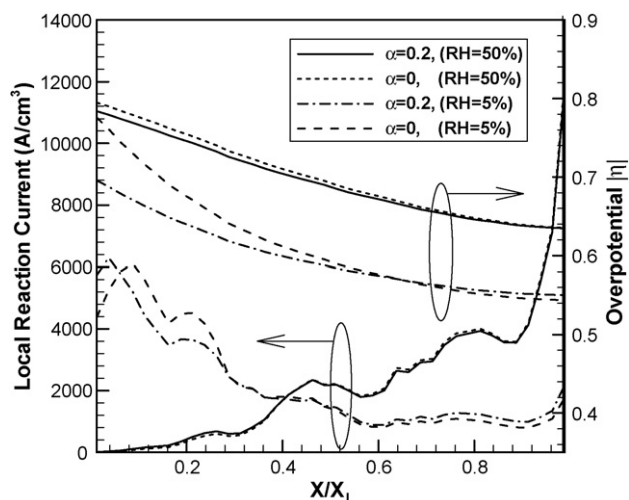


Fig. 10. Local reaction current and overpotential distributions across the thickness of the catalyst layer for different net water transport coefficients.

further illustrated in Fig. 10, which exhibits the reaction current and overpotential distributions. For the inlet humidity of 50%, the reaction current and overpotential distributions remain unaltered by the value of α . But for the cathode inlet humidity of 5%, due to the higher oxygen concentration, the reaction zone tends to be mainly concentrated toward the front end of the catalyst layer i.e. closer to the membrane–CL interface. The corresponding oxygen concentration fields are shown in Fig. 11 to provide further evidence.

In summary, the DNS results clearly show that at 5% RH there is a considerable increase in the cathode voltage loss as α is reduced to zero. Again, this is due to the lower water activity thus leading to the lower proton conductivity of the electrolyte phase. The lower proton conductivity would push the reaction zone to the front end, consuming more oxygen there. The larger consumption rate of oxygen, in turn, reduces the oxygen concentration there, which eventually requires a larger overpotential to drive the reaction. It can be observed that the difference in the reaction rate near the membrane–CL interface, shown in Fig. 10, is closely correlated to the difference in the local oxygen concentration shown in Fig. 11, which leads to higher total cathode voltage loss with α being zero. This study clearly suggests that at low cathode inlet RH, restraining the back diffusion of water to the anode side is important and can significantly improve the cathode performance with the better-hydrated electrolyte phase.

3.4. Optimization of the catalyst layer composition

In order to investigate the effect of electrode composition on cathode performance, a series of simulations with various combinations of pore and electrolyte volume fractions are carried out and the predicted polarization curves are presented in Fig. 12. It can be observed that the greater the pore volume fraction, the larger the mass transport limiting current density. This is quite obvious, since the oxygen transfer to the active reaction sites would benefit from a large number of open pores available for transport.

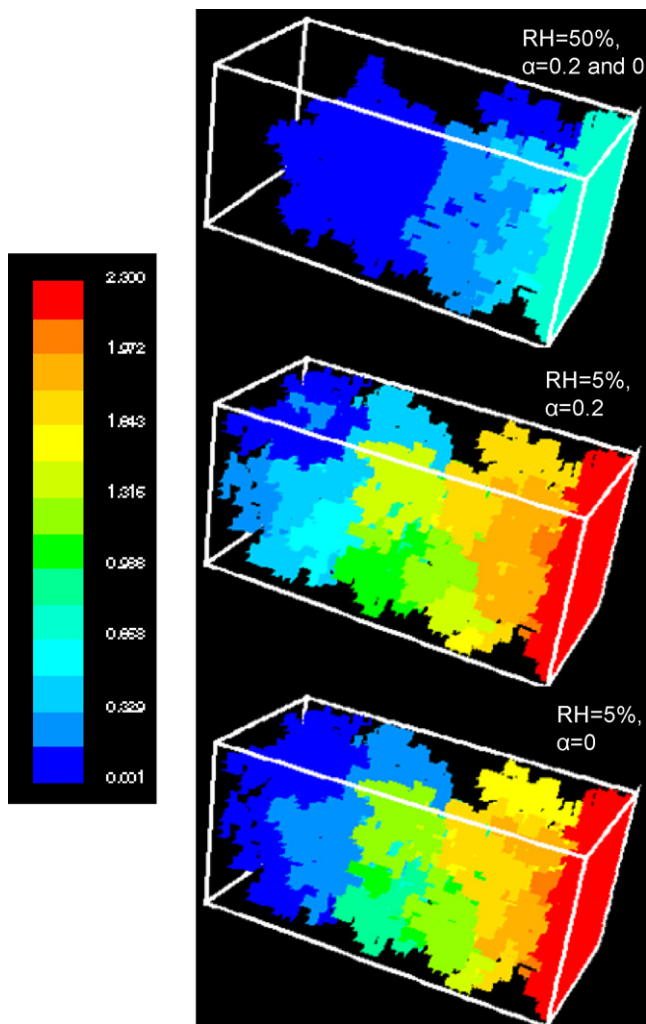


Fig. 11. 3-D oxygen concentration contours at 2.3 A/cm^2 under various combinations of inlet humidity and net water transport coefficient.

Fig. 13 shows the oxygen concentration distributions in the catalyst layer microstructure with different pore volume fractions corresponding to that described in Fig. 12. The operating current density is 2.3 A/cm^2 , corresponding to the mass transport limiting regime. It can be seen that with the same consumption rate, the oxygen concentration gradient is relatively smaller with pore volume fraction of 0.6. When the porosity is decreased further thereby increasing the relative volume fractions of the electrolyte and electronic phases, the oxygen concentration gradient becomes steeper. At porosities of 0.34 and 0.36, the oxygen concentration gradient becomes steep enough that the pores in the vicinity of the membrane are depleted with oxygen, thus leading to a dramatic increase in the voltage loss at high current densities, as shown in Fig. 12. It can also be found from Fig. 12 that as the porosity is slightly decreased from 0.36 to 0.34, the performance of the catalyst layer becomes worse over a wider range of current densities. This is because as the porosity approaches the percolation threshold (approximately 0.3), both the effective porosity and active interfacial area reduce drastically leading to significant decline in the electrode performance [17].

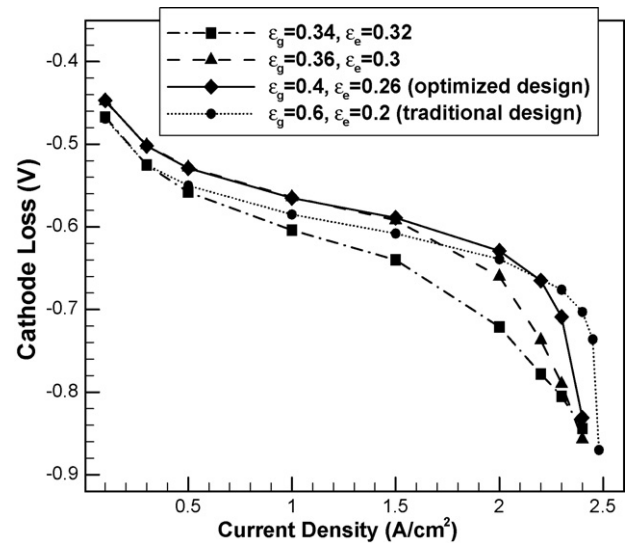


Fig. 12. Polarizations curves for different void and electrolyte volume fractions.

Fig. 14 shows the cross-section averaged distribution of “transport” pore volume fraction along the CL thickness. Horizontal lines indicate the corresponding average nominal porosities in consistency with that considered in Fig. 12. At the porosity of 0.6, it is evident that the “transport” pores are distributed randomly around the nominal porosity, indicating that there are few “dead” pores. As the porosity decreases, the difference between “transport” pore volume fraction and nominal porosity becomes larger, as expected. At porosity of 0.34, the relative fraction of “transport” pores becomes very small. Obviously, such a small effective porosity not only causes hindered oxygen transport but also leads to reduced electrochemically active interfacial area. More importantly, since the microstructure is generated purely randomly, Fig. 14 shows that at porosity of 0.34 there are effectively no “transport” pores in the region close to the membrane although the nominal porosity is greater than the percolation threshold. It renders oxygen to be inaccessible to the region close to the membrane and leads to oxygen depletion-like situation otherwise occurring at large current densities. The combined effect of these two factors might lead to severe decline in cathode performance at small low porosities.

Therefore, the pore volume fraction should be kept large enough to avoid the percolation effect. However, when the porosity is increased from 0.4 to 0.6 at the expense of reducing electrolyte/electronic phase volume fractions, the polarization curve does not show improved performance except that the ohmic control regime is slightly extended. In contrast, the voltage loss in the ohmic control regime increases due to the lower electrolyte phase volume fraction. In order to obtain optimal composition of the cathode catalyst layer for best performance, detailed predictions are presented in Fig. 15 for different combinations of pore and electrolyte volume fractions.

Fig. 15 shows the local reaction current and overpotential distributions at current density of 0.5 A/cm^2 . As explained earlier, with pore and electrolyte phase volume fractions of 0.34 and 0.32, respectively, the resulting small amount of “transport” pores make the region near the membrane almost inaccessible

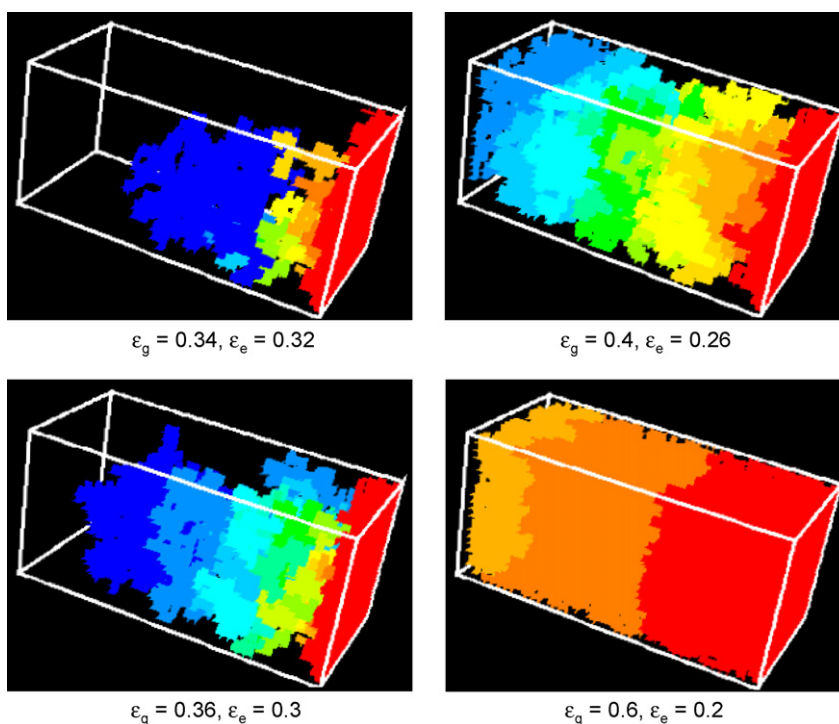


Fig. 13. 3-D oxygen concentration contours at various pore and electrolyte volume fractions in the transport limited regime.

to oxygen. The increased loss is then due to the ionic current passing through the region close to the membrane–CL interface without reaction; the resistance being much lower to pass current through the electronic phase after the charge transfer reaction. As the porosity is increased, from 0.36 to 0.4, there is marginal performance improvement, which is due to the larger reaction area available with porosity of 0.4. With pore volume fraction of 0.6, Fig. 15 shows that the reaction is mainly concentrated in the vicinity of the membrane–CL interface, which indicates significant decrease in proton conductivity. This is once again

due to the reduced electrolyte volume fraction to 0.2, which is typically used in the design of the conventional catalyst layers.

In summary, by assuming a sufficiently large electronic conductivity of the Pt/C phase and a fixed electronic phase volume fraction, it is important to select an appropriate pore to electrolyte phase volume fraction ratio in order to achieve the best performance of the cathode CL. In general, both the pore and electrolyte phase volume fractions should be larger than the percolation threshold. With this constraint, further increase in the pore and electrolyte phase volume fractions will relax the mass transport limitation and reduce the ohmic drop, respectively. Hence, there exists an optimal CL composition

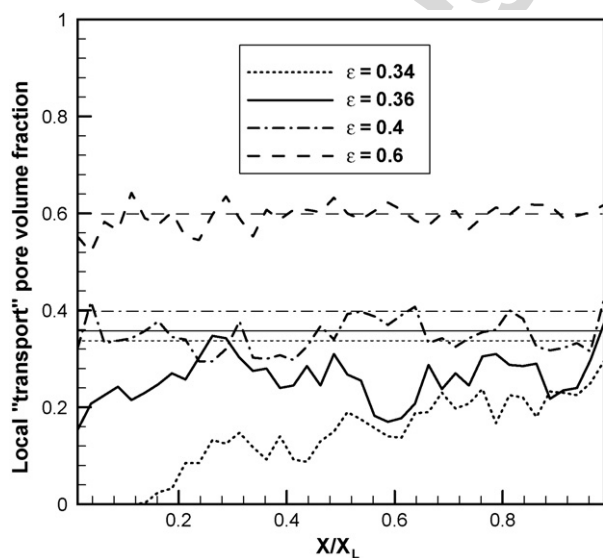


Fig. 14. Local "transport" pore distributions related to different porosities. The straight lines indicate the corresponding nominal porosity.

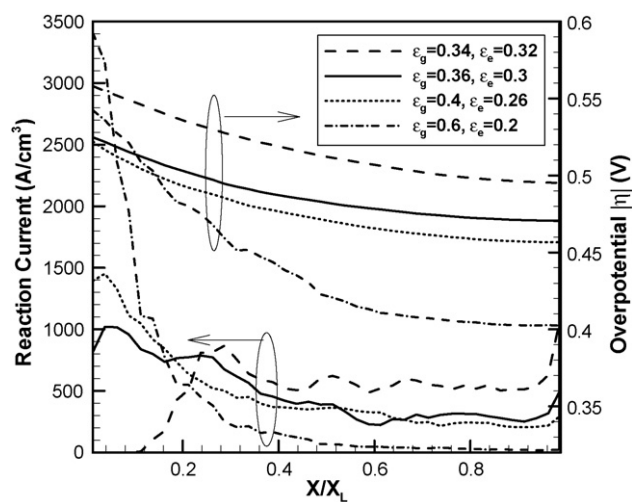


Fig. 15. Reaction current and overpotential distributions across the catalyst layer thickness at 0.5 A/cm² for various pore and electrolyte volume fractions.

for the best performance. According to the present DNS model calculations, the optimal CL compositions could be evaluated as 0.4 and 0.26 for the pore and electrolyte phase volume fractions, respectively. In comparison, the traditional CL design with the electrolyte volume fraction of 0.2 results in higher ionic resistance, while a relatively large porosity does not benefit the cathode performance much, other than slightly delaying the mass transport control regime.

4. Conclusions

The PEFC cathode CL requires a delicate balance between oxygen diffusion and proton conduction for higher cell performance, which entails careful optimization of the CL composition in terms of its constituent phase volume fractions. This study investigates the influence of the electrolyte and void phase fractions on the electrode performance as well as the interdependence between the CL composition and the cell operating conditions. In this regard, a direct numerical simulation (DNS) model is developed which solves point-wise accurate charge and species transport equations on a random, purely disordered catalyst layer microstructure. The influence of the inlet RH and the net water transport from the anode, on the cathode performance is elucidated which indicates the dependence of the operating conditions on the CL composition. Finally, the DNS model predicts an optimum composition of the catalyst layer with pore volume fraction of 0.4 and electrolyte volume fraction of 0.26 for the best performance. The present DNS model, therefore, underscores its viability as a fast screening tool for the design and development of high-performance catalyst layers using a systematic science-based approach.

Acknowledgement

Funding of this work by ECEC industrial sponsors is gratefully acknowledged.

Appendix A

a	specific interfacial area (cm^2/cm^3)
c_i	local concentration of species i (mol/m^3)
D_i	diffusion coefficient of species i (m^2/s)
f	phase function for the single domain approach
F	Faraday's constant (96,487 C/mol)
i	molar flux of species i ($\text{mol}/\text{m}^2 \text{ s}$)
I	current density (A/cm^2)
j	reaction current density (A/cm^2)
n_d	electro-osmotic drag coefficient
p	pressure (Pa)
R	universal gas constant (8.314 J/mol K)
RH	relative humidity
S	source term in the governing equations
T	absolute temperature (K)
x	x coordinate (μm)
y	y coordinate (μm)
z	z coordinate (μm)

Greek letters

α	net water transport coefficient
α_c	cathodic transfer coefficient
ε_k	volume fraction of phase, k , in the catalyst layer
ϕ_k	electrical potential in phase k (V)
κ	electrolyte conductivity (S/m)
λ	membrane water content ($\text{mol H}_2\text{O}/\text{mol SO}_3^-$)

Subscripts and superscripts

e	electrolyte phase
eff	effective
g	gas phase
GDL	gas diffusion layer
inlet	gas channel inlet
L	catalyst layer thickness
net	net value
O_2	oxygen
prod	water production in the cathode catalyst layer
ref	reference value
sat	saturation of water
w	water
0	boundary value at the CL–GDL interface or initial/intrinsic value

References

- [1] T.E. Springer, S. Gottesfeld, Modeling of Batteries and Fuel Cells, in: R.E. White (Ed.), The Electrochemical Society Proceedings, 1991, p. 197.
- [2] M.L. Perry, J. Newman, E.J. Cairns, J. Electrochem. Soc. 145 (1998) 5.
- [3] M. Eikerling, A.A. Kornyshev, J. Electroanal. Chem. 453 (1998) 89.
- [4] S. Um, C.Y. Wang, K.S. Chen, J. Electrochem. Soc. 147 (2000) 4485.
- [5] S. Um, C.Y. Wang, J. Power Sources 125 (2004) 40.
- [6] Y. Wang, C.Y. Wang, Electrochim. Acta 50 (2005) 1307.
- [7] T. Berning, D.M. Lu, N. Djilali, J. Power Sources 106 (2002) 284.
- [8] S. Mazumder, J.V. Cole, J. Electrochem. Soc. 150 (2003) A1503.
- [9] C.Y. Wang, Chem. Rev. 104 (2004) 4727.
- [10] M. Eikerling, A.A. Kornyshev, J. Electroanal. Chem. 475 (1999) 107.
- [11] C. Marr, X.G. Li, J. Power Sources 77 (1999) 17.
- [12] D.T. Song, Q.P. Wang, Z.S. Liu, T. Navessin, M. Eikerling, S. Holdcroft, J. Power Sources 126 (2004) 104.
- [13] Q.P. Wang, M. Eikerling, D.T. Song, Z.S. Liu, T. Navessin, Z. Xie, S. Holdcroft, J. Electrochem. Soc. 151 (2004) A950.
- [14] O. Antoine, Y. Bultel, P. Ozil, R. Durand, Electrochim. Acta 45 (2000) 4493.
- [15] D. Song, Q. Wang, Z. Liu, T. Navessin, S. Holdcroft, Electrochim. Acta 50 (2004) 731.
- [16] G. Wang, P.P. Mukherjee, C.Y. Wang, Electrochim. Acta 51 (2006) 3139.
- [17] G. Wang, P.P. Mukherjee, C.Y. Wang, Electrochim. Acta 51 (2006) 3151.
- [18] P.P. Mukherjee, C.Y. Wang, J. Electrochem. Soc. 153 (2006) A840.
- [19] S. Gottesfeld, T.A. Zawodzinski, in: C. Tobias (Ed.), Advances in Electrochemical Science and Engineering, vol. 5, Wiley and Sons, New York, 1997.
- [20] P.M. Adler, Porous Media: geometry and transports, Butterworth-Heinemann, Stoneham, MA, 1992.
- [21] T.A. Zawodzinski, J. Davey, J. Valerio, S. Gottesfeld, Electrochim. Acta 40 (1995) 297.
- [22] R.B. Bird, W.E. Stewart, E.N. Lightfoot, Transport Phenomena, second ed., Wiley, New York, 2002.
- [23] T.E. Springer, T.A. Zawodzinski, S. Gottesfeld, J. Electrochem. Soc. 138 (1991) 2334.
- [24] S.V. Patankar, Numerical Heat Transfer and Fluid Flow, Hemisphere, Washington, DC (1980).
- [25] Fluent 6.1 UDF Manual, Ansys-Fluent, NH, USA.